

https://dspace.org/

Hydraulic fracturing potential of tight gas reservoirs A case study from a gas field in the Bredasdorp Basin South Africa

Sithembele Zangqa; Eric Saffou; R Gholami; U Zimmermann; A Raza ...

https://hdl.handle.net/10539/40687
WOS

Downloaded from a DSpace repository. https://dspace.org/

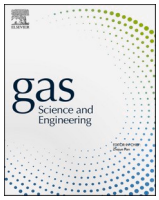
128 (2024) 205364



Contents lists available at ScienceDirect

Gas Science and Engineering

journal homepage: www.journals.elsevier.com/gas-science-and-engineering



Hydraulic fracturing potential of tight gas reservoirs: A case study from a gas field in the Bredasdorp Basin, South Africa

Sithembele Zangqa [a], Eric Saffou [a,*], Raoof Gholami [b], Udo Zimmermann [b], Arshad Raza [c], Musa S.D. Manzi [a], Ray Durrheim [a]

[a] School of Geosciences, University of the Witwatersrand Johannesburg, South Africa
[b] Department of Energy Resources, University of Stavanger, Norway
[c] Department of Petroleum Engineering, College of Petroleum and Geosciences, King Fahd University of Petroleum and Minerals, Saudi Arabia

ARTICLE INFO

Keywords:
Hydraulic fracturing
Tight gas
South Africa
Characterisation
Geomechanics

ABSTRACT

The issue of hydraulic fracturing in the onshore Karoo Basin has triggered an intense political, social and environmental debate in South Africa. This research paper proposes the relatively under-explored F–O tight gas field in South Africa as a demonstration site that can shed light on the ongoing debate on the use of hydraulic fracturing in the Karoo Basin. By combining petrographic and geomechanical analyses with critical velocity experiments and rock mechanics testing, a step-by-step guide for assessing the hydraulic fracturing potential of tight gas reservoirs was presented. K-Means clustering was used to improve the sampling strategy and to capture reservoir heterogeneity. The results obtained showed that K-Means clustering improves reservoir characterisation by revealing heterogeneous intervals, thus optimising petrographic and geomechanical analyses. In addition, the hydraulic fracturing fluid was found not to cause formation damage in the reservoir at a critical velocity of 0.155 ml/min. The elastic properties also showed that the F–O Tight Gas Field has a high degree of brittleness with good hydraulic fracturing potential. Finally, the characterisation of the fractures shows that partially open fractures are prevalent, which can dilate under the high differential stresses in the reservoir. Although further investigation is required, this study has shown that the F–O gas field is a promising candidate for hydraulic fracturing.

1. Introduction

Hydraulic fracturing, also known as fracking, is a topic of intense political, social, and environmental debate in South Africa. In the 1960s, SOEKOR (Southern Oil Exploration Corporation) carried out extensive drilling in the Karoo region to determine its potential for hydrocarbon resources. Later analyses of the Karoo shale revealed that it mainly contains natural gas with low permeability and porosity (Haughton et al., 1953; Pietersen et al., 2021; Rowsell and de Swardt, 1976; Winter et al., 1970). Since 2007, South Africa has been exploring the application of hydraulic fracturing technology to extract shale gas in the Karoo region. However, due to environmental concerns (Kissinger et al., 2013), these exploration efforts have been significantly delayed to date. One of the biggest risks associated with this technology is the potential contamination of groundwater (Chisebe, 2017), which is vital for agriculture in the Karoo region. In light of the recent energy crisis in South Africa and the global shift towards green energy, South Africa is now reconsidering its stance on whether or not to proceed with hydraulic fracturing in the Karoo Basin.

South Africa could also explore the development of a tight gas reservoir in the Bredasdorp Basin. This basin is the subject of ongoing exploration and production activities that include the evaluation of oil and gas fields for engineered carbon storage (Saffou et al., 2022). Unfortunately, the reserves of the Bredasdorp Basin which is part of the F–O gas field have been somewhat overlooked due to its limited porosity and permeability. The F–O gas field was originally identified as an area with the potential for economically viable gas production following the discovery of gas in the sandstone reservoirs during petrophysical and geochemical analyses (Godongwana et al., 2009; Simonis and Sontundu, 2010). However, despite these discoveries, the wells were eventually abandoned due to the low porosity (2%–18%) and poor permeability (0.1–10 mD) of the reservoir (Higgs, 2009; Kathleen et al., 2009). The F–O tight gas field as a primary source of natural gas supply in South Africa does not necessarily eliminate the risks associated with hydraulic

* Corresponding author.
E-mail address: eric.saffou@gmail.com (E. Saffou).

https://doi.org/10.1016/j.jgsce.2024.205364
Received 7 January 2024; Received in revised form 15 April 2024; Accepted 29 May 2024
Available online 4 June 2024
2949-9089/© 2024 Elsevier B.V. All rights are reserved, including those for text and data mining, AI training, and similar technologies.

fracturing fluid contamination. It does, however, have the potential to contaminate water resources in the Karoo region.

Hydraulic fracturing of tight gas reservoirs has been extensively studied in the literature. For instance, Kumar et al. (2022) developed a geomechanical model for fractures to identify sweet zones and barriers in three different tight reservoirs deposited between continental and shallow marine environments. The model was created by integrating wellbore breakouts and enhanced acoustic data. Data from rock mechanics tests were used to calibrate the elastic properties, while the authors were unable to calibrate the horizontal stress as no data from leak-off tests or minifrac were available. Zones with low permeability were also found to have higher tensile strength, resulting in high fracture initiation pressure. Tang et al. (2021) designed a hydraulic fracturing experiment to evaluate the damage mechanism of tight sandstone cores of the Lower Jurassic Ahe Formation in Dibei in the Kuqa Depression of the Tarim Basin. The authors emphasised that the degree of damage to the permeability of tight sandstone by fracking fluid is moderate to weak. Rahman et al. (2021) investigated the propagation of hydraulic fracturing in heterogeneous tight gas reservoirs in the Middle East by considering different parameters for fracturing design and well placement. The results of the study showed that the natural orientation of the fractures has a significant impact on the final geometry and network of hydraulic fractures. Since hydraulic fracturing is a geomechanical process, integrating geomechanical parameters such as stress, rock mechanical properties, and fracture toughness would have improved the results. Zhang et al. (2021) designed an experimental model to evaluate the influence of cemented fractures on the propagation of hydraulic fractures in tight sandstones. The effect of the cemented fractures is evaluated using triaxial hydraulic fracturing experiments with acoustic emission monitoring technology. Depending on the angle between the cemented natural and hydraulic fractures, the authors proposed four interaction behaviours: Deflection I ($0^\circ \pm 15^\circ$), Deflection II and Penetration ($90^\circ \pm 15^\circ$) and composite ($45^\circ \pm 15^\circ$) behaviours. Although validation of in-situ data remains essential, the insights gained in this study, combined with numerical simulations, have the potential to provide reliable models for hydraulic fracturing propagation. Dou et al. (2021) explored the optimization of hydraulic fracturing parameters for tight sandstone reservoirs, focusing on fluid flow, net pressure balance, and displacement through simulation. Their findings suggested that an optimal construction fluid volume of 1800 m^3, a displacement rate of 16 m^3/min, and a perforation count of 36–48 are recommended, balancing the net pressure of fracture and wellbore friction. Liu et al. (2022) utilized various geological data sources to conduct numerical simulations investigating the impact of the thickness of low-permeability interbedded sandstone and mudstone on hydraulic fracture propagation in the Ansai district of the Ordos Basin. They found that longitudinal fractures can cross the mudstone layers when a 3–5 m thick sandstone is overlain by a less than 0.3 m thick mudstone, resulting in extensive fractures. Conversely, thin sandstone layers (<1.5 m thick) overlain by mudstone thicker than 0.8 m limit the fracture propagation to the underlying sandstone body. Yan et al. (2022) used true triaxial simulation experiments on artificially unconsolidated rocks to investigate the factors that influence the fracture initiation and shape of fractures during hydraulic fracturing. Their results indicate that in unconsolidated rocks, high injection rates are necessary for fracture initiation due to the permeability and the low strength of rocks, which is associated with a lower fracture pressure under reduced effective stress conditions.

Having said that, little attention has been given to the characterisation of the hydraulic fracturing potential of tight gas fields. Most research on hydraulic fracturing relies primarily on numerical simulations as the only means of investigating the relevant questions (Yang and Gao, 2022; Xiong and Ma, 2022; Kanin et al., 2021; Rathnaweera et al., 2020; Salimzadeh et al., 2020; Yaobin et al., 2020; Wang, 2019; Xu et al., 2019; Chen et al., 2018; Xie et al., 2018; Wang et al., 2018; Guo et al., 2015; Zhang et al., 2015). However, this research paper argues that the integration of geological and geomechanical analyses provides early insights into the hydraulic fracturing potential of tight gas fields. In addition, critical points can be identified in the preliminary characterisation phase that need to be further investigated using numerical methods. Therefore, it is crucial to understand both the geological and geomechanical properties of the targeted tight gas reservoirs in order to optimise the hydraulic fracturing design and create robust simulation models to predict the propagation of hydraulic fractures, and thus mitigate the risks associated with this technology. This paper proposes a stepwise methodology to investigate the potential of tight gas reservoirs for hydraulic fracturing. The F–O gas field in South Africa's Bredasdorp Basin is used as a case study to bring new perspectives to the ongoing discussion on the adoption of hydraulic fracturing in South Africa.

2. Geological settings

The late Jurassic period witnessed the fragmentation of the Gondwana supercontinent, which led to the formation of dextral transtension tectonics on its southwestern margin. These tectonic processes played a crucial role in the formation of the Late Mesozoic Outeniqua Basin, which consists of a series of separate sub-basins, including the Bredasdorp Basin (see Fig. 1). The break-up of Gondwana took place along zones of weakened lithosphere, as Will and Frimmel (2018) pointed out. Extensive research on hot spots and linear, fixed, and active volcanism in the ocean basin have shown that igneous events played a significant role in facilitating the break-up (Duncan, 1981; Will and Frimmel, 2018; Duncan et al., 1997). Davies (1997) argued that rifting began earlier in eastern South Africa than in western South Africa. Rifting occurred along the right-lateral strike-slip fault zone, referred to as the Agulhas-Falkland dextral transform fault (Ben-Avraham et al., 1993; Thomas, 1993Scrutton and Dingle, 1976; Reeves and De Wit, 2000; Johnston, 2000; Paton, 2006; Stankiewicz et al., 2008; Kuhlmann et al., 2010; Jokat and Hagen, 2017). The extensional fault system observed in southern Africa, which can be attributed to continental rifting, extends over a length of 480 km. It consists of fault arrays, with the maximum length of the fault segments reaching 230 km and a fault displacement of up to 16 km (Paton, 2006). These boundary faults are characterised by a listric shape and dip between 40° and 60° in the WNW-ESE direction (McKenzie and Jackson, 1983; Paton, 2006). In contrast to the typical echelon pattern of most extensional systems, the fault segments in this region exhibit a co-linear geometry (Paton, 2006). While the regional WNW-ESE trend is observed in the Late Mesozoic basin faults, the Bredasdorp Basin has adapted to a NW-SE trend (Davies, 1997). Several studies have found that the steep compressional faults in the Palaeozoic Cape Fold Belt were reactivated as normal faults during Mesozoic extension (Shone et al., 1990; Bate et al., 1992; De Wit and Ransome, 1992; Booth and Shone, 2002; Paton, 2006).

The tectonic and metamorphic processes that led to the formation of the present-day bedrock of Bredasdorp include the deposition and deformation of the Neoproterozoic to Early Cambrian successions (Wildman et al., 2015). Both were deformed during the Pan-African orogeny from the Neoproterozoic to the Early Ordovician (Wildman et al., 2015). The deposition of the Cape and Karoo Supergroups, which form the basement of the Bredasdorp Basin, was preceded by the intrusion of the Cape Granite Suite into the Ediacaran to Lower Paleozoic rocks of the Malmesbury Group (Johnston, 2000). The Cape Fold Belt deformed the sediments of the Cape Supergroup, while affecting only the lower units of the Karoo Supergroup. This deformation took place as the Karoo Foreland Basin developed from the end of the Paleozoic to possibly the early Mesozoic (Tankard et al., 2009). Tectonic activity, subsidence and eustasy subsequently influenced the sediment accretion in the Bredasdorp Basin. Two major periods of sediment accumulation are recognised in the literature: (i) Syn-Rift 1 and (ii) Syn-Rift 2. Syn-Rift 1 is characterised by continental clastic and fluvial/lacustrine sediments (Hirsch et al., 2009) derived from transgressive and regressive cycles (Mcmillan et al., 1997). Sediment

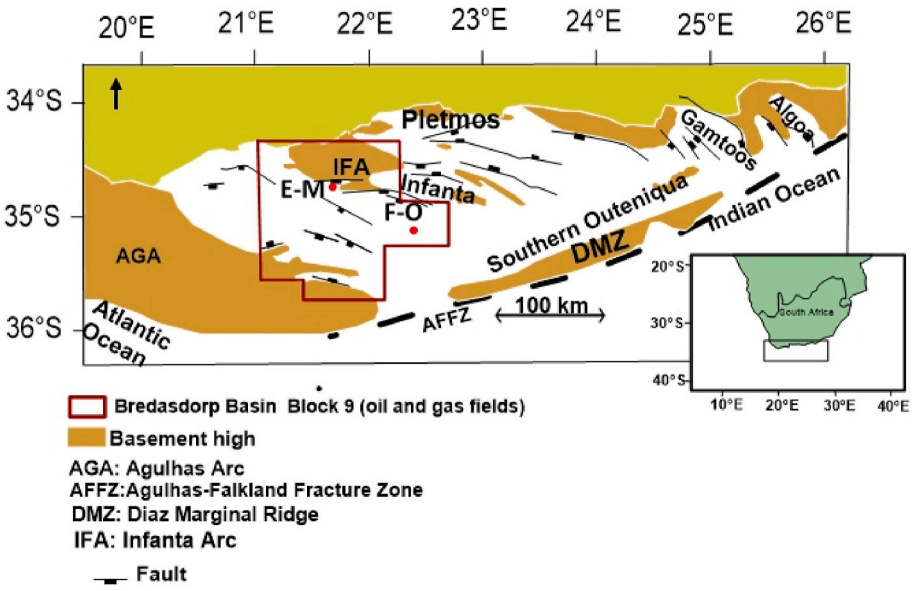


Fig. 1. Structural map of the Bredasdorp Basin. The red block and red points indicate the location of F–O and E-M gas fields in the Bredasdorp Basin. The F–O gas field is located to south-east of the E-M gas field, closer to the Agulhas-Falkland Fracture Zone (AFFZ).

accumulation was mainly controlled by faults at the drift boundary. A recent U–Pb chronostratigraphic study of the Uitenhage Group syn-rift sediments from the Southern Cape of South Africa shows that syn-rift sedimentation began in the Jurassic and extended until the Early Cretaceous (Muir et al., 2020). Brown et al. (2014) found evidence of a cooling period in the Late Cretaceous that accelerated the early rifting erosion responsible for the sediments of the basin fill. Eroded siliciclastics and shale of the Cape Supergroup and sandstones and shales of the Karoo Supergroup are the sources of the Syn-Rift clastic deposits. Mcmillan et al. (1997) classified the Syn-Rift 1 sequences in the gas fields as lower fluvial, lower shallow marine, upper fluvial and upper shallow marine sequences. According to the authors, the lower fluvial sequence, which was deposited in alluvial fans and broad floodplains, consists of red and green argillites. The lower shallow-marine sequence is characterised by thick glauconite shallow-marine shoreface sandstone. The shoreface sandstone is bioturbated with ostracodes, ooliths, shell debris, and foraminifera. Bioturbation can either improve or reduce the reservoir quality (Baniak et al., 2015; Joel and Eswaran, 2015). The upper fluvial sequence can be recognised by the presence of fine upward trends. The primary lithologies consist of interbedded non-glauconitic sandstones, siltstones and green claystones deposited in an alluvial flood plain of a fluvial channel. Finally, the upper shallow marine area, which shows an upward coarsening trend, is mainly characterised by thick glauconitic sandstones. The Syn-Rift 2 or drifting sedimentation is tectonically more complicated than the Syn-Rift 1 sequence. The deposition of Syn-Rift 2 sediments is outlined by several unconformities created by tectonic readjustments in the basin (Tinker et al., 2008). Mcmillan et al. (1997) and McMillan (2003) have discussed the regional unconformities of the Bredasdorp Basin in detail. The late Valanginian period is dominated by low-oxygen conditions that favour the deposition of black claystone and turbiditic sandstone. The latter extends to the Early Barremian (6At1). The period of sediment accumulation from the late Valanginian (1At1) to the early Aptian (13At1) is characterised by the occurrence of channels and canyons that cut through the Syn-rift 1 sediments and formed traps for hydrocarbons. Earlier aptian channels and Middle Albian sandstones overlying 14At1 are oil-bearing reservoirs. Rich organic claystone deposits in low-oxygen environments predominate in the Upper Cenomanian (15At1).

3. Methodology

In order to determine the hydraulic fracturing potential of the F–O gas field, petrographic analyses, rock mechanical investigations, stress analyses, fracture characterisation and hydraulic fracturing-related tests were integrated. The data set of six exploration wells (T-O1, T-O2, T-O3, T-O4, T-O6 and T-O8) with geophysical logs (gamma ray and image logs), core samples and geological reports were provided by PetroSA (Petroleum Oil and Gas Cooperation of South Africa) and PASA (Petroleum Agency of South Africa).

3.1. Reservoir characterisation

3.1.1. Sampling method

Gamma ray logs from four wells (T-01, T-02, T-03 and T-04) from a tight gas field in the Bredasdorp Basin were cluster analysed using Techlog® 2019 (Schlumberger software) to assess the lateral and vertical heterogeneity of the reservoir and overburden units. The overburden formations are included in the analysis as they are often evaluated in terms of potential for hydraulic fracture height growth and wellbore stability. The result provides information to improve the selection of core sections for petrographic analyses and rock mechanics testing. This process identifies rock units with unique properties and thus increases the efficiency of laboratory tests and analyses. Table 1 shows the sampling carried out for this study using cluster analysis. Samples were then selected according to the availability of drill core.

3.1.2. Petrographic and fine migration

SEM, XRD, core and petrographic analyses were then carried out to

Table 1
Cluster units derived from cluster analysis with rock type, and sample IDs.

Cluster colors	Rock Type	Sampling Well Choice	Depth (m)	Sample ID
Dark Blue	Shale	T-O3	3702.69	PSA 22-1
Red	Sandstone	T-O3	3713.67	PSA 20-3
Green	Sandstone	T-O2	3668.28	PSA 21-5
Brown	Sandstone	T-O4	3740.24	PSA 10-7
Yellow	Sandstone	T-O4	3740.96	PSA 19-3
Light Blue	Siltsone	T-O3	3758.75	PSA 23-7

characterise the clusters and understand the microlithic variations associated with the sandstone reservoir of interest. The texture of the rocks in the reservoir was analysed based on characteristics such as grain size composition, sorting, matrix, and cement. The quantifications from the modal analysis were then plotted on Folk's (1980) QFR diagram (Fig. 3c) to categorise the mineral framework of each cluster unit. The petrophysical properties of the clusters were then determined by routine plug analyses and mercury injections. Routine plug analysis measures two important parameters: grain density and nitrogen gas permeability. Gas permeability was measured at an effective net stress of 15 MPa.

During production in tight gas reservoirs, fine migration can occur when small solid particles are detached from the surface of clays, illite, silt, quartz, and feldspar by the flowing fluids. They can reduce permeability as the moving fine particles clog narrow pore throats. To investigate whether the fine migration in the F–O gas field is significant, a critical velocity test was performed. In this test, the flow rate or velocity of a fluid is gradually increased from a stable and initially low baseline rate. The fine migration is determined by observing a decrease in the permeability of the sample as the flow rate is increased above the baseline level. In this study, a sample from well T-O1 with a diameter of 2.53 cm and a length of 2.88 cm with a porosity of 13.25 % and a gas permeability of 0.42 mD at dry saturation was used. The pore system was evacuated for about 10 min and then flooded with 2% KCl brine. At ambient temperature (21 °C), a net confining and back pressure of 16.54 MPa and 1.38 MPa, respectively, was applied. Flow rates of 0.082, 0.117 and 0.155 ml/min were maintained for 100 min. After each period of increased flow rate, the rate was then reduced to the initial level of 0.043 ml/min for comparison.

3.2. Geomechanical characterisation

3.2.1. Rock mechanical testing

Rock mechanical tests were performed on the cluster units to determine the mechanical properties of the different cluster units and to compare their geomechanical response to loading. Triaxial compression tests were performed on vertically orientated core samples of 5.34 cm length and 2.54 cm diameter from shales and sandstones with a length to diameter ratio of approximately 2. To avoid abrupt irregularities on the upper and lower cylindrical surfaces, the end faces of the samples were cut and polished parallel to each other and at right angles to the longitudinal axis. In addition, the flatness of the samples was checked with a dial gauge according to the standards recommended by the ISRM (ISRM, 1983). In addition, the samples were encased in plastic sleeves that served as an impermeable membrane to prevent contamination of the sample by the confining fluid (Fig. 6). The experiments were carried out at room temperature and a constant confining pressure (drain condition) of 0 MPa. Strain gauges were attached to the samples to measure the axial and lateral strain. The deviatoric stress was applied to the surface of the sample at a constant displacement rate of 0.5 MPa/min. At a confining pressure of 0 MPa during the triaxial test, the Unconfined Compression Strength (UCS) was determined.

The Brazilian tests of each cluster were carried out for tensile strength tests on the core samples with a length of 1.27 cm and a diameter of 2.54 cm in the shale and a length of 1.91 cm and a diameter of 3.81 cm in the sandstone, with an overall length-to-diameter ratio of approximately 0.5. To account for the anisotropy of dark blue, the core samples were orientated parallel, perpendicular and at an angle of 45° to the bedding during the test. Thus, the tensile strength of the dark blue cluster (shale) was evaluated in three different orientations: perpendicular, parallel and 45° to the bedding.

3.2.2. In-situ stress magnitudes

In an offshore area, the overburden stress (s_v) is calculated by the integration of the formation density from the surface to the reservoir depth , z, as expressed by (Zoback et al., 2003):

$$s_v = \rho_w g z_w + \int_o^z \rho(z) g dz \approx \rho_w g z_w + \overline{\rho} g (z - z_w) \quad (1)$$

In the above equation, ρ_w is the density of the water, z_w is the water depth, $\rho(z)$ is the formation density as a function of depth, g is the gravitational acceleration, $\overline{\rho}$ is the mean overburden density, and z is the formation depth. In contrast to leak-off tests, which are typically performed at the casing shoe, minifrac tests provide a much better insight into the magnitude of the least principal stress as they are carried out at the reservoir interval. The minifrac data recorded in well T-O4 at a depth of 3811 m was used to estimate the magnitude of the minimum horizontal stress. The stress polygon was used to estimate the maximum horizontal stress (SHmax) based on the borehole breakouts and tensile fractures (Zoback et al., 2003). In this case, well T-O2 was considered, no breakouts and tensile fractures were observed.

3.2.3. Fracture characterisation and fracture toughness

The Formation Microscanner Imager (FMI) was used to map fractures in the caprock and reservoir in the T-O8 well, which extend from 3418 to 3781.5 m and from 3914 to 3739 m depth respectively. The 3D Mohr diagram was used to evaluate the stability of each fracture type based on the geomechanical parameters and in-situ stresses. Fracture toughness is a material property of rock that describes the resistance to fracture propagation. The burst test is one of the most commonly used techniques for measuring fracture toughness. In this study, pre-notched thick-walled cylinder samples from borehole T-O4 at a depth of 3702.16 m (shale) and 3744 m (sandstone) were subjected to internal pressure in a triaxial cell until failure. The fracture toughness (KIC) was determined using the following equation (Abou-Sayed, 1978):

$$K_{IC} = K_I^{*J} P_i \sqrt{\pi a} \quad (2)$$

where K_I^{*J} is the local minimum of stress intensity factor coefficient, a is an inner radius, and P_i is the sample burst internal pressure value. K_I^{*J} is a function of the non-dimensional crack length, the ratio of the sample radius, and the inner hole sample radius. Fig. 2 summarises the methodology used in this study.

4. Results

4.1. Reservoir characterisation

Fig. 3a displays the gamma-ray logs of well T-04, T-03, T-02, and T-01, which were used to perform the cluster analysis. The yellow colour indicates the sandstone, while the brown colour indicates shale Processing of the gamma-ray logs produced the cluster analysis results shown in Fig. 3b. Seven cluster units were predicted from the K- Means cluster analysis of the gamma-ray logs from wells T-O1, T-O2, T-O3 and T-O4. The analysis identified dark blue (shale) and light blue (siltstone) in the overburden formation. On the other hand, yellow, green, red, brown, and black clusters were recognised in the reservoir. The black cluster was not analysed further as it is less abundant than the others. In addition, the study focused on significant clusters as the number of available drill cores was limited. In Fig. 3c, the QFR diagram of Folk's (1980) reveals a sublitharenite composition for the dark blue cluster and a lithic arkose composition for the green, red and brown clusters, while the light blue and yellow clusters are classified as feldspathic litharenites. Based on the petrographic analyses, different lithotypes were defined to match the six cluster units, which are addressed in the following sections.

4.1.1. Medium grain lithic arkose (red cluster units)

The rock of the red cluster unit is more densely packed than that of the first unit. The matrix is almost absent. Sorting is moderate or bimodal, with medium-sized sand grains being the most abundant,

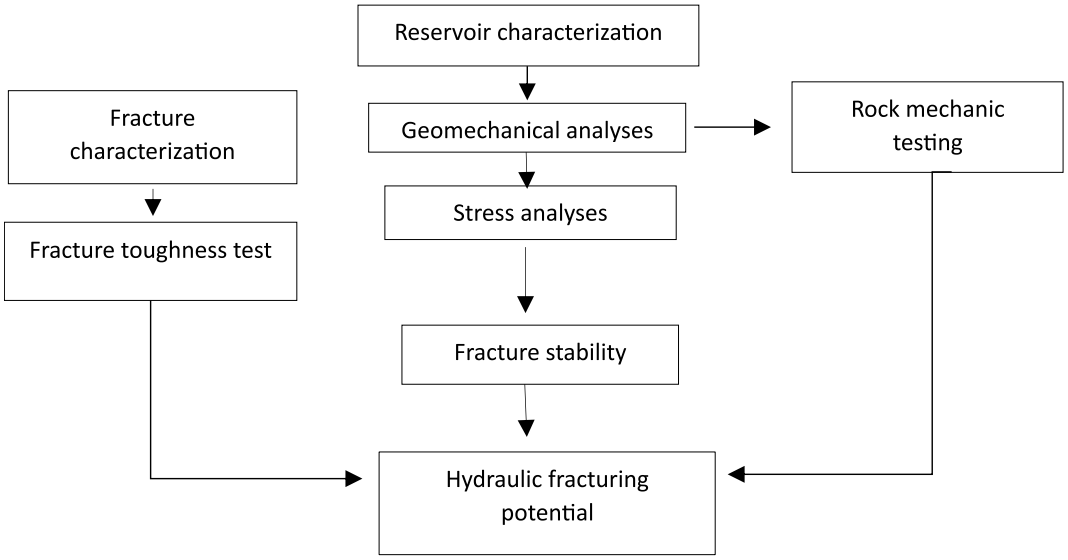


Fig. 2. The workflow used to evaluate hydraulic fracturing potential of tight gas reservoirs.

together with very fine-grained sand. The grains are semi-circular to round, and the most common mineral is quartz. Alkali feldspar occurs, but lithoclasts are rare. Intrabasinal clasts are common, including coral fragments, some of which are partially dolomitised. Chlorite is abundant in narrow contact zones between some grains. The grain boundaries are often characterised by pressure solution and are cemented. Calcite and dolomite are the predominant cementing minerals that reduce intergranular porosity (Table 2). Fig. 4a shows that authigenic illite and chlorite contribute to the reduction in porosity. The red cluster has the lowest porosity (8.71 %) and a permeability of 0.157 mD, as given in Table 3.

4.1.2. *Fine grain lithic arkose (green cluster unit)*

The rocks of the green cluster unit are texturally and mineralogically quite variable. A medium sand grain size dominates, but smaller grains are abundant. The large fraction consists mainly of subrounded and some subangular clasts. Quartz is the most abundant mineral, followed by alkali feldspar. Plagioclase appears as small but euhedral grains within the matrix. The proportion of matrix is about 15%, although it is difficult to define as there is a large grain size variability caused by poor sorting with a grain size range from fine sand to silt. Chert and volcanic lithoclasts are common, which is distinctly different from the other cluster units. Only a few grains show clear and diagenetic contact areas. The rocks appear to be texturally less mature than most of the others and less affected by diagenesis. Nevertheless, the feldspars are altered, and chlorite is even visible as larger grains, so it is not authigenic. Moldic pores resulting from the dissolution of feldspars and rock fragments are widespread in the green cluster. Ferroan calcite and dolomite are also present (Table 2). SEM analyses (Fig. 4b) show the image of a moldic pore filled with mixed clays with chlorite crystals on the left side of the pore. Despite the presence of dissolution pores, the green cluster has a lower porosity than the brown cluster but a higher permeability than the other clusters (Table 3).

4.1.3. *Medium grain lithic arkose (brown cluster unit)*

The rock of the brown cluster unit consists of fine to medium-grain sandstone. The matrix is rare and is mostly less than 5%. The grains are subangular to subrounded; only a few are well-rounded or strictly angular. This is the reason for the most abundant mineral, quartz and alkali feldspar (Table 2). Plagioclase is rare and strongly altered. Metasedimentary lithoclasts are common, as are gneissic grains. All grains show substantial alteration and diagenetic structures at the edges of the grains, which can be attributed to the pressure solution. Clay and very small grains of mica are present. SEM revealed the presence of illite, chlorite and large euhedral overgrowths of quartz crystals sealing intergranular voids (Fig. 4c). Table 3 shows that the porosity and permeability of the brown cluster are 12% and 0.164 mD, respectively.

4.1.4. *Medium grain feldspathic litharenite (yellow cluster unit)*

The samples from the yellow cluster unit are relatively poorly sorted and consist of very fine to medium size sand. The variety of grains is large; besides quartz, altered alkali feldspar occurs, and a number of lithoclasts are even of volcanic origin. The rocks are arenites, and the matrix is quite low (<5 %). The grains are mainly subrounded or subangular and have a broken appearance. Pressure solution is common. Fine-grained material is absent, as is pseudomatrix. The presence of abundant intergranular pores dominates the yellow cluster. The intergranular pores are obtained by lining the clay pores and coating the grains to prevent the growth of quartz cement. Fig. 4d shows the intergranular space partially occluded by quartz overgrowth and pseudohexagonal chlorite crystals. In addition, the yellow cluster has the highest porosity (13%) and permeability of 0.310 mD (see Table 3).

4.1.5. *Medium sand arenites to wackes (light blue cluster unit)*

The rock is poorly sorted, but a medium sand size dominates the samples. The grains are angular to semi-circular. The main mineral is quartz, followed by alkali feldspar. The latter is often strongly altered. A few lithoclasts are of metamorphic origin (quartz and chlorite schist) while those of sedimentary origin (fine grain sandstone) are common. Depending on the area, the matrix accounts for a maximum of 15–20% and consists of ferruginous phases, clay minerals and quartz (Table 2). Some areas show typical characteristics of a pseudomatrix with ghost structures of sedimentary lithoclasts. Organic material occurs along the grain boundaries, but no preferred orientation of the fragments can be recognised. The rocks are texturally immature.

4.1.6. *Fine grain sand-to siltstone (dark blue cluster unit)*

The rocks are characterised by poor sorting and a large number of well-rounded to angular grains. The samples show soft-sedimentary structures with pockets of siltstone surrounded by sandy areas, so-called flasher structures. The finer silty areas are dominated by quartz, iron oxides and clay with some feldspars (Table 2). The sandy areas show a wide variety of grain shapes and sizes and contain considerable organic matter, mostly in the form of elongated flakes that appear to have a preferred orientation. As the rock is not metamorphosed and there is no visible deformation, this can be related to sedimentation and/

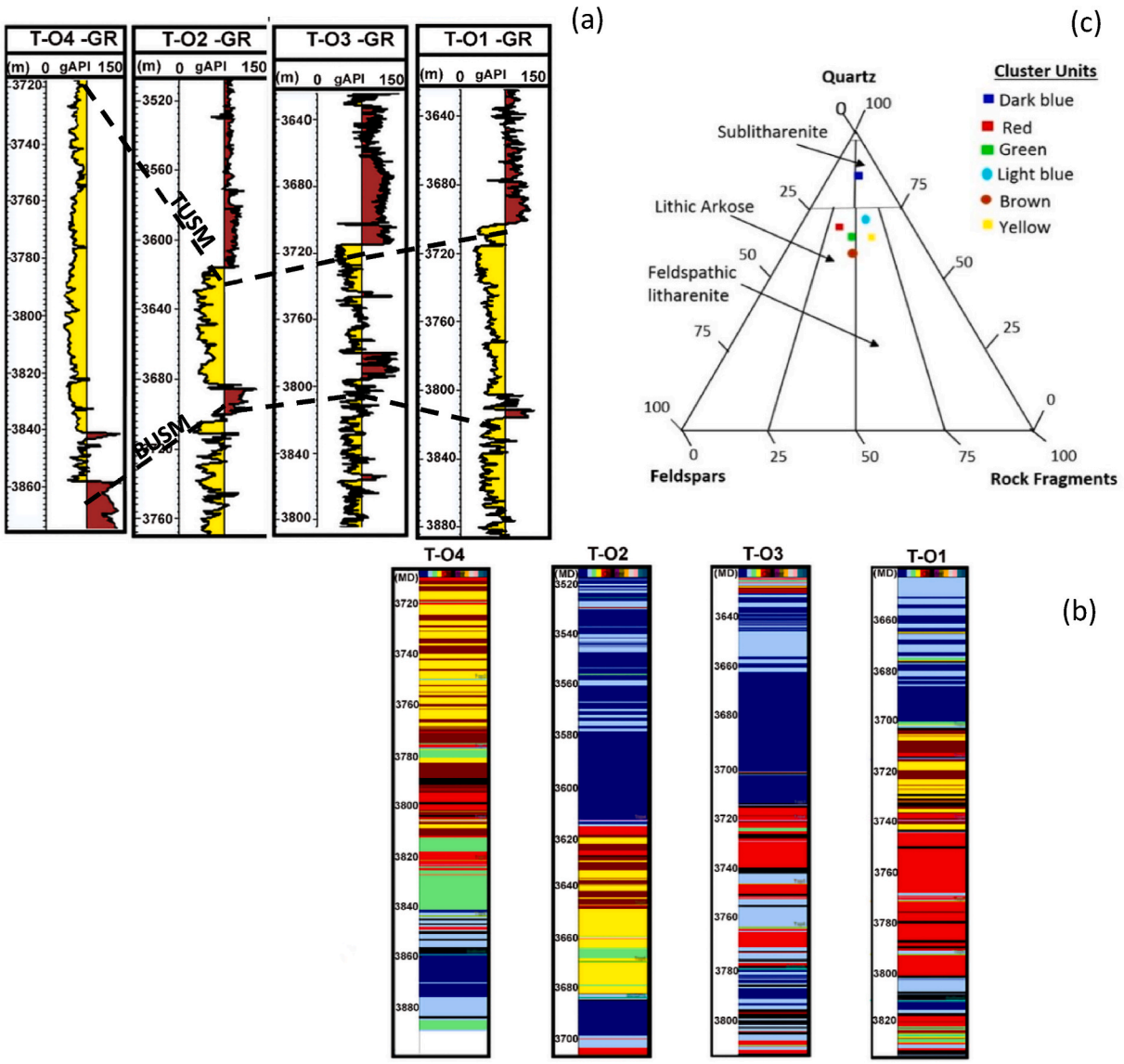


Fig. 3. a) Gamma-rays of wells T-01, T-O2, T-O3 and T-O4 were processed with the K-means clustering algorithm between TUSM (Top Upper Shallow Marine) and BUSM (Base Upper Shallow Marine), (b) Clustering shows six clusters as the main cluster units, sandstone (red, yellow, green, brown), siltstone (light blue) and claystone (dark blue), and c) QFR triangular classification (after Folk (1980)) of cluster units based on a mineralogical framework red, green, and brown cluster units are categorised as lithic arkose while yellow cluster is categorised as feldspathic litharenite.

Table 2
XRD analysis and mineral composition of the cluster units.

%	Dark Blue	Red	Green	Brown	Yellow	Light Blue
Quartz	36	80	81	86	85	63
k-feldspar	2	3	3	3	1	6
Plagioclase	6	4	7	5	7	11
Calcite	3	5	0	1	0	2
Siderite	1	0	0	0	0	0
Fe-dol	2	3	1	1	1	1
Pyrite	1	0	0	0	0	0
Barite	1	0	1	0	0	0
Illite/smectite	13	1	0	2	0	4
Illite + mica	26	1	0	2	0	4
Kaolinite	2	0	1	0	1	0
Chlorite	7	1	3	2	2	4

or diagenesis. Large muscovite crystals show the same orientation. Lithoclasts are extremely rare and, if abundant, may have dissolved into a pseudomatrix.

4.2. Fine migration

Migration of fine particles can occur as they detach from the surfaces of clays, silt, quartz, and feldspar due to fluid flow. This process may lead to reduced permeability as the mobile fines obstruct narrow pore passages. Fig. 5 shows the result of the critical velocity measurements where no significant reduction in the permeability was observed. Therefore, the fine migration should not cause any damage to the formation during production.

4.3. Geomechanical characterisation

4.3.1. Rock mechanical testing

Fig. 6 shows the post-failure of the core samples used for the triaxial testing while Fig. 7 left shows the axial stress versus axial strain curves for the green cluster. The curve highlights the linear elastic part (in red) of the stress-strain plots used to estimate Young's modulus. Fig. 7 on the right shows the average radial strain versus axial strain for the green cluster from which the Poisson's ratio was derived. As with the stress/

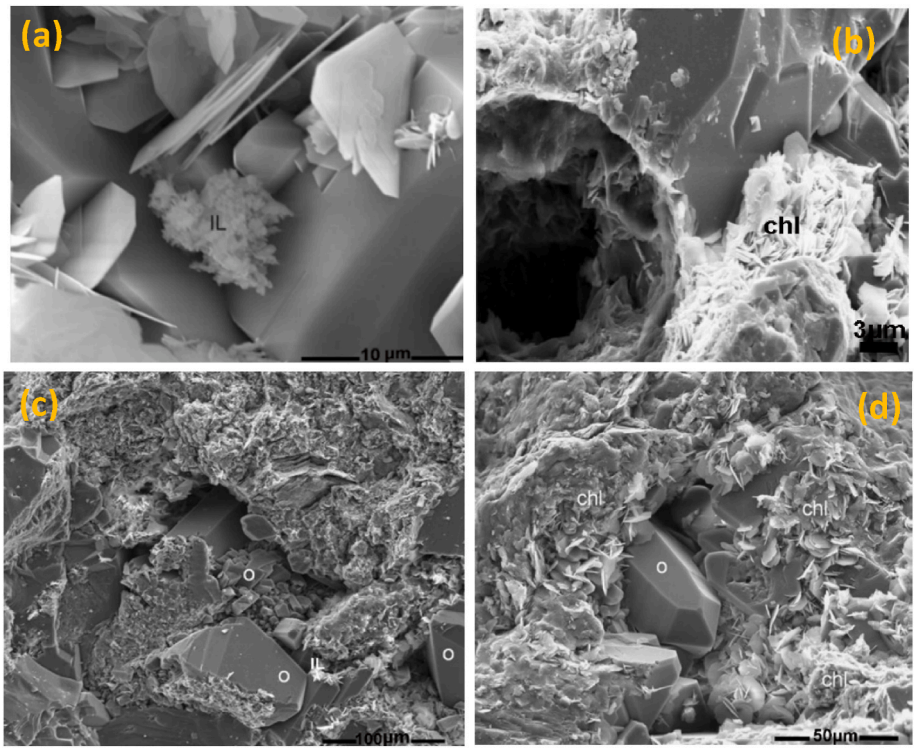


Fig. 4. (a) Red cluster (lithic arkose) showing coated grain with a small euhedral pseudohexagonal chlorite crystal (chl) with smaller illite (IL) aggregates at the centre. (b) Green cluster (lithic arkose) showing a pore filled with mixed phyllosilicates like massive chlorite (chl). (c) Brown cluster (lithic arkose) shows intergranular space between two quartz grains is reduced by the growth of quartz cement (o) and, minor illite (IL) and chlorite (chl). (d) Yellow cluster (feldspathic litharenite) showing intergranular space partially occluded by the new growth of quartz (o) and chlorite (chl).

Table 3
Petrophysical properties of the cluster units.

Cluster Units	samples	Grain density (g/cm^3)	Mercury porosity (%)	Gas Permeability (mD)	Net Effective Stress (MPa)
Yellow	PSA 19-3	2.682	13.00	0.310	15
Red	PSA 20-3	2.661	8.71	0.157	15
Brown	PSA 10-7	2.693	12.00	0.164	15
Green	PSA 21-5	2.666	10.00	0.508	15

strain curves, the red part of the curves was used to calculate the Poisson's ratio for the corresponding confining pressure.

Table 4 gives the elastic and strength properties of the cluster units. The UCS varies between 80 and 172 MPa, with the highest and lowest values given by the red (172 MPa) and yellow (80 MPa) clusters, respectively. The Poisson's ratio, in turn, is between 0.11 and 0.23, with the yellow cluster showing the highest value for the Poisson's ratio (0.23) and the dark blue and light blue clusters showing intermediate values.

Table 5 gives the value of the tensile strength obtained from different samples. As can be seen in this table, the red cluster has the highest tensile strength (7.5 MPa), while brown, green, and yellow have a similar tensile strength. Fig. 8 shows cross plots of Poisson's ratio versus Young's modulus indicating the Brittle/Ductile behaviour of the clusters.

As can be seen in Fig. 8, all clusters fall into the range of brittle behaviour. However, the green and light blue clusters show a very high brittle behaviour compared to the red, brown, and yellow clusters. It is important to note that the dark blue cluster, which was identified as shale, also exhibits brittle behaviour.

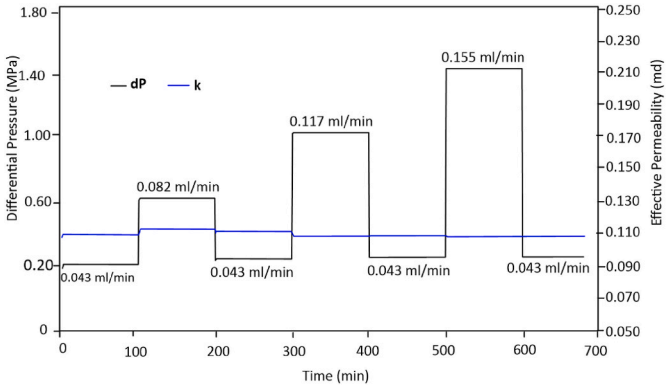


Fig. 5. Critical fluid flow velocities of a sample from well T-01 at a depth of 3728 m. The black graph in histogram form indicates the flow rate, and the blue line displays the change in permeability. No significant permeability reduction was observed.

4.3.2. Fracture toughness

The results obtained from the fracture toughness tests indicated that the burst pressure of the shale sample taken from the depth of 3704.16 m was 15.19 MPa, which corresponds to a fracture toughness (KIC) of 0.64 MPa(m)$^{0.5}$. A fracture toughness (KIC) of 0.89 MPa(m)$^{0.5}$ was also obtained for the sandstone sample taken from the depth of 3744.40 m. Table 6 gives the parameters used to estimate the fracture toughness for shale and sandstone samples.

(1). Non dimensional crack length

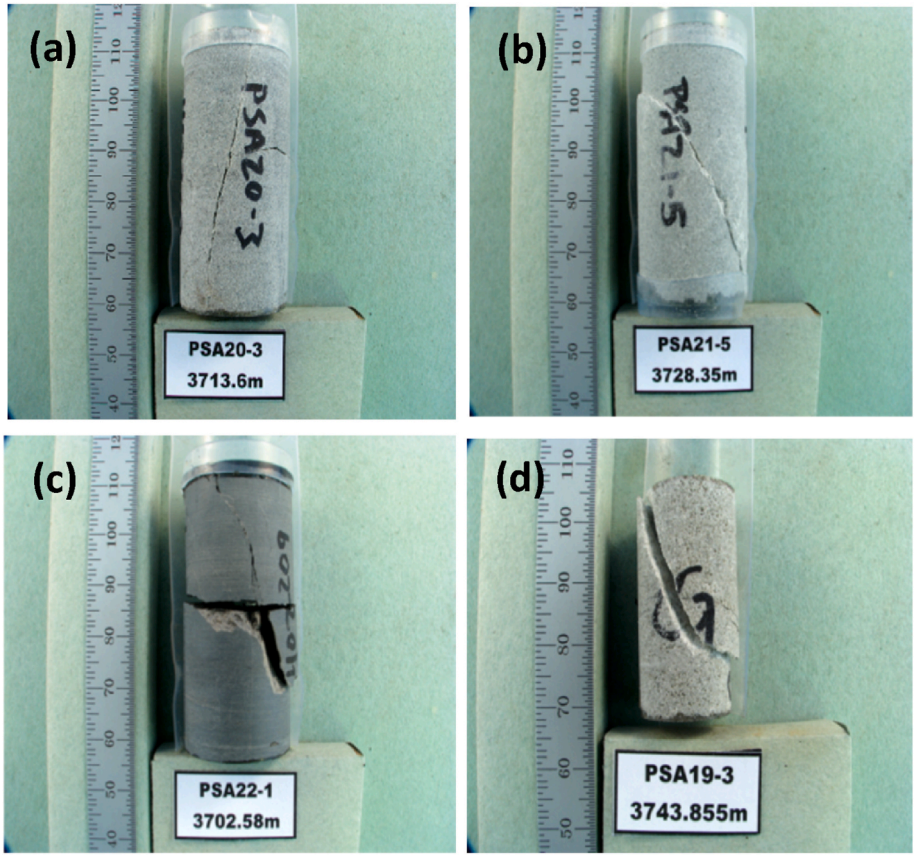


Fig. 6. Triaxial test samples: (a) red cluster, (b) green cluster, (c) dark blue cluster, and (d) yellow cluster.

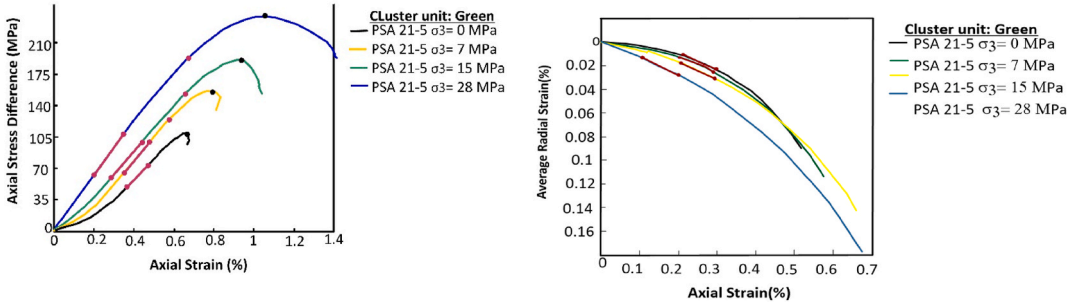


Fig. 7. Left) Axial stress difference versus axial strain measured during triaxial compression testing of feldspathic litharenite sample (green cluster unit). Right) Averaged radial strain versus axial strain, measured during triaxial compression testing of feldspathic litharenite sample (green cluster).

Table 4
Elastic and strength Properties of the cluster units at 0 MPa confining pressure.

Sample ID	Cluster colour	UCS (MPa)	Young's modulus (GPa)	Poisson's ratio
PSA 22–1	Dark Blue	121	20,340	0.12
PSA 20–5	Red	172	32,819	0.13
PSA 21–1	Green	108	21,100	0.10
PSA 10–7	Brown	110	22,752	0.17
PSA 19–7	Yellow	80	18,202	0.23
PSA 23–7	Light Blue	147	16,616	0.11

Table 5
The indirect (Brazilian) tensile strength tests performed on the cluster units.

Lithotype	Orientation	Tensile (MPa)
Dark Blue (Shale)	Perpendicular	5.2
	Parallel	4
	45°	1.8
Yellow Cluster		4.5
Green Cluster		4.6
Red Cluster		7.5
Brown Cluster		5.1

4.4. In-situ stress magnitudes

The overburden stress estimated using Eq. (1) gave a gradient of 0.02 MPa/m at a depth of 3800 m for wells T-O1, T-O2 and T-O3.

4.4.1. Minimum horizontal stress

The minifrac data recorded in well T-O4 at a depth of 3811 m are given in Table 7. It appeared that the breakdown pressure or fracture initiation is higher in the first cycle (97.70 MPa) than in the second cycle when the fracture is reopened because the tensile strength component

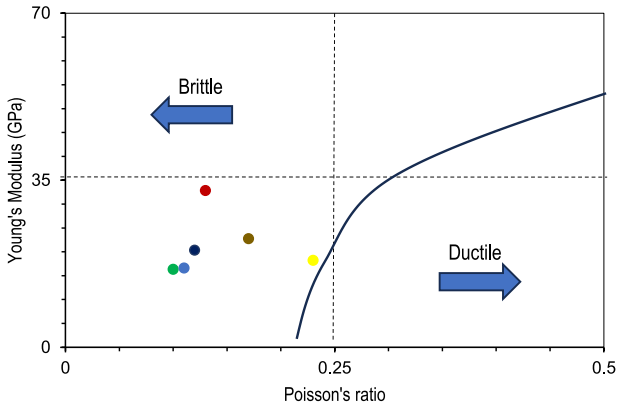


Fig. 8. Cross-plot of Poisson's ratio versus Young's modulus indicating Brittle/Ductile behaviour of the clusters (adapted from Grieser and Jun Bray (2007)). The green cluster displays a very good brittle behaviour while yellow cluster exhibits poor brittle behaviour close to the ductile line. Arrows show the direction of increase in the ductile/brittle behaviour.

has been removed. Therefore, the pressure difference between the breakdown pressures observed in the first cycle and fracture reopening pressure in the second cycle can serve as a reasonable estimate of the tensile strength, which in this particular case was 5.7 MPa. This value was closely aligned with the measurements from the Brazilian test, described earlier in Table 5. The closure pressure is often considered as the magnitude of the minimum horizontal stress. As the data does not provide a value for the fracture closure pressure, the initial shut-in pressure of 73 MPa was used as the upper boundary for the minimum horizontal stress.

According to the geological reports, the direction of the minimum horizontal stress measured from breakouts in wells T-O1 and T-O3 varies from N110° to N170° in the overburden and from N140° to N145° at the depth of the reservoir.

4.4.2. Maximum horizontal stress

The stress polygon was used to estimate the maximum horizontal stress (SHmax) based on the borehole breakouts and tensile fractures (Zoback et al., 2003). In this case, well T-O2 was considered but there was no breakouts and tensile fractures observed. Therefore, the upper boundary of SHmax was assumed to be equal to the magnitude of the unconfined compressive strength at the depth of interest (Saffou et al., 2022). The stress polygon was then constructed for the depth of 3800 m where minifrac data was available. Fig. 9 shows the stress polygon obtained from Well T-O2.

The initial pore pressure of the reservoir, which was obtained from the well test of T-O2 at a depth of 3800 m, was 53.43 MPa. The purple line in Fig. 9 represents the compressive strength value and corresponds to the UCS of the green cluster identified at 3800 m in well T-O2 (see Table 4). The blue line indicates the minimum horizontal stress obtained from the minifrac tests while the yellow lines correspond to the tensile strength values, which fall between 0 and 4.6. It was then found that the lower and upper boundary of SHmax are 95 MPa and 108 MPa, respectively. Looking at the vertical and minimum horizontal stresses, it seems that the region is dominated by a normal/strike-slip faulting regime. Table 8 summarises the in-situ stress values of the F–O gas field.

4.5. Fracture classification and stability

The fracture density appeared to be low and is generally in the ENE-WSW direction (see Fig. 10a, b and 10c). The density plots were derived from the true dip and azimuth ratio and showed the orientation of the fracture density. Resistive fractures were identified at a depth of 3426.45–3777.78 m, with sinusoidal anomalies indicating that the fractures are closed. The high-density resistive fracture (True dip/Azimuth = 1) had a dip toward the southwest (see Fig. 10a). In contrast, the conductive fractures have dark, sinusoidal anomalies, indicating that the fractures are open.

Only very few fractures show a conductive character with no

Table 7
Minifrac test results of Well T-O4 at 3811 m.

Cycle	Fracture reopening pressure (MPa)	Fracture Propagation (MPa)	Initial shut-in Pressure (MPa)
1	–	83.43	75
2	86.18	82.73	73
3	84.46	82.73	74.46
4	82.73	82.73	73

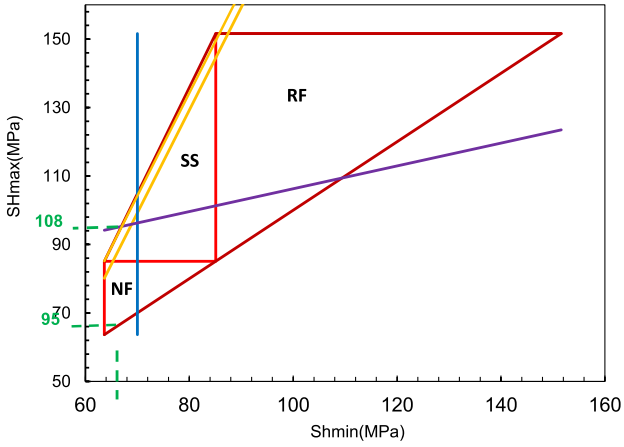


Fig. 9. Stress polygon of well T-O2 at a depth of 3800 with a reservoir pore pressure of 53.43 MPa, vertical stress of 85 MPa, and unconfined compressive strength of 108 MPa. The purple line represents the unconfined compressive strength of the green cluster, and the yellow lines represent the tensile strength of the rock (4.6 MPa). The vertical blue line represents the value of the Shmin estimated from the minifrac tests, while the green dashed line represents the possible maximum horizontal stress values (95 MPa–108 MPa). The stress polygon indicates a normal/strike-slip regime.

Table 8
Pore pressure and in-situ stresses of well T-O2 in the F–O gas field.

	Depth (m)	PP (MPa)	Sv (MPa)	SHmax (MPa)	Shmin (MPa)
Caprock	3700	51.8	81.4	92.5–103.6	66.6
Reservoir	3800	53.43	85	95–108	70
	Gradient (MPa/m)	0.014	0.022	0.025–0.028	0.018

Table 6
Fracture toughness of the reservoir and neighbouring layers in F–O gas field.

Depth (m)	Lithology	Sample length	Sample radius(m)	Inner hole radius (m)	$I^{(1)}$	K_i^{*j}	Burst pressure (MPa)	K_{IC} MPa(m)$^{0.5}$
3702.16	Shale	0.056	0.032	0.0032	0.239	0.42	15.19	0.64
3744.40	Sandstone	0.063	0.032	0.0032	0.245	0.42	21.04	0.89

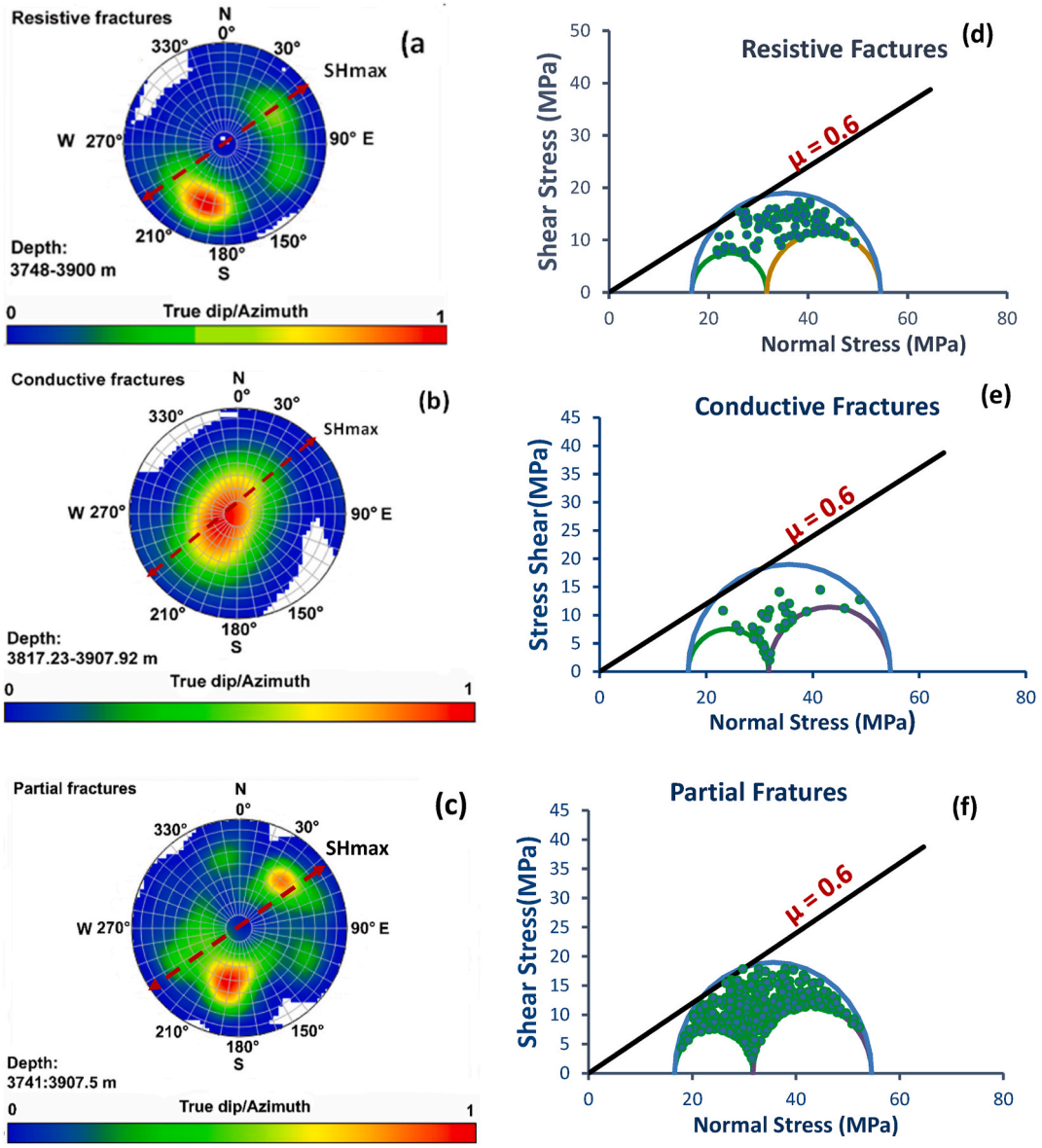


Fig. 10. Fracture classification and stability. (a) High density stereoplot for Resistive fractures with a dip of 50°-90° toward southwest. (b) High density stereoplot for Conductive fractures with a dip between 0°-50° toward northeast, 10°-80° toward southwest and 30°-60° toward northwest. (c) High density stereoplot for Partial fractures with a dip between 30° to 50° and 0° to 30° toward northeast and southwest, respectively and 3D Mohr diagram assessing fracture stability for Resistive fractures (d), Conductive fractures (e) and Partial fractures (f) The red dotted line represents the direction of the maximum horizontal stress (SHmax).

preferred direction but dip randomly toward the northeast, southwest and northwest. Partial fractures exhibit both resistive and conductive properties. These fractures had a dip towards the northeast and southwest (see Fig. 10c). The 3D Mohr diagram was used to assess the stability of each fracture type based on the geomechanical parameters and in-situ stresses determined earlier (Sv = 85.1 MPa, Shmin = 70 MPa, SHmax = 108 MPa, PP = 53.4 MPa, friction coefficient of 0.6) (see Fig. 10d, e and 10f). In general, resistive, conductive, and partial fractures are stable under the current normal/strike-slip faulting regime. However, some partial fractures with a dip of 65°–81° NW touched the failure envelope line and may become unstable (see Fig. 10).

5. Discussion

5.1. Reservoir characterisation

In this paper, an attempt was made to investigate the hydraulic fracture potential of a tight gas reservoir in the Bredasdorp Basin, South Africa, by integrating reservoir characterisation with geomechanical and fracture parameters. The K-Means clustering method was used to decode and capture the heterogeneity of the reservoir. The folk classification approach then categorises the green, red and brown clusters as lithic arkose sandstone and the light blue and yellow clusters as feldspathic litharenite sandstone, indicating an identical tectonic provenance but different mineral composition (Sun et al., 2020; Chima et al., 2018a, 2018b). Each cluster exhibits unique potential controlled by the presence or absence of cement, clays and intergranular and moldic pore networks, as well as the presence of organics along with pyrite, indicating anoxic environments that facilitate the preservation of organics. Of these clusters, the yellow cluster unit was found to have a higher reservoir potential than the other sandstone cluster units as it has a well-preserved intergranular pore network with a porosity of 13%, while the red cluster has the lowest reservoir potential with a pore network clogged by authigenic cement. In contrast, the yellow cluster unit provides fragile lithoclasts that can alter and create secondary porosity and a pseudo-matrix that allows fluid migration.

The critical velocity experiment was performed with a 2% KCl brine for a total duration of 300 min to evaluate the potential for formation damage. No significant reduction in permeability was observed at the critical flow rate of 0.155 ml/min. The results of the XRD analysis (Table 2) revealed that calcite and dolomite are the predominant cement while authigenic chlorite, illite and kaolinite are the main clay minerals (see Fig. 4) in the clusters. It should be noted that kaolinite and illite are particularly prone to migrate as fine particles (Hibbeler et al., 2003). Therefore, at high flow rates of more than 0.155 ml/min, there is a risk that kaolinite deflocculates or that illite, which breaks easily due to its fibrous morphology, clogs the pore spaces (Yang et al., 2016; Byrne et al., 2014). The illite/smectite clay fraction appears in dark blue (13%), light blue (4%), red (1%) and brown (2%) clusters (Table 2).

5.2. Geomechanical analyses

The geomechanical model of the F–O gas field described in Section 4.4 revealed an overburden stress gradient of 0.022 MPa/m, a minimum stress gradient of 0.018 MPa/m and a maximum horizontal stress gradient between 0.025 and 0.028 MPa/m. These results indicate that the stress regime in the F–O gas field is dominated by a normal/strike-slip fault regime. Saffou et al. (2020, 2023) have also estimated the stress gradients in the EM gas field in the Bredasdorp Basin to be 0.022 MPa/m for the overburden stress, 0.016 MPa/m and 0.018 MPa/m for the minimum horizontal and maximum horizontal stress gradients, respectively. These results are consistent with previous studies showing that the development of the Bredasdorp Basin is due to dextral trans-tension tectonics. The rifting event responsible for the formation of the Bredasdorp Basin occurred on a right-lateral strike-slip fault zone known as the Agulhas-Falkland dextral transform fault (Jokat and Hagen, 2017; Kuhlmann et al., 2010; Ankiewicz et al., 2008; Reeves and De Wit, 2000; Ben-Avraham et al., 1993). It is, therefore, reasonable to assume that the strike-slip tectonic activity influenced the in-situ stresses in the F–O gas field in Southern Africa during the Early Cretaceous. The fact that the F–O gas field is located further south in the vicinity of the Agulhas Fracture Zone, which has its origin in the dextral Agulhas-Falkland Transform Fault, further supports the above observations.

A normal/strike-slip faulting regime also indicates that hydraulic fractures will propagate vertically (Hudson and Matson, 2012; King et al., 1957). The direction of minimum horizontal stress at a depth of the reservoir is between N140° and N145°. In addition, the significant stress difference of 25–37 MPa (obtained from the 0.007–0,01 MPa/m stress gradients difference of the reservoir rock reported in Table 8) at 3800 m indicates that the resulting hydraulic fractures are likely to have well-orientated, long, and planar fractures (Zheng et al., 2020; Simonson et al., 1978).

The elastic properties derived from the triaxial tests were plotted to investigate the brittleness and ductility of the tight reservoir. Brittleness and ductility are critical in the design of a hydraulic fracture treatment as they control the length and shape of the fracture (Khan et al., 2018). The cross-plot analysis reveals that all clusters are located within the brittle zone. This indicates that the reservoir has a high degree of brittleness, making it a promising candidate for hydraulic fracturing (Hou et al., 2015; Bill and Jun, 2007). However, it is essential to emphasize that the presence of interlayers of siltstone (light blue cluster) and shale (dark blue cluster) can have both advantages and disadvantages. These interlayers can facilitate fracture propagation but can also pose challenges in terms of fracture height containment. This argument is further supported by the burst experiment, in which the fracture toughness was estimated. As highlighted, the fracture toughness measured in the bounding formation (shale) or caprock was 0.64 $MPa(m)^{0.5}$, while the fracture toughness of the pay zone (sandstone) was 0.89 $MPa(m)^{0.5}$. The contrast in fracture toughness between the pay zone and the neighbouring formations shows that the fracture will most likely propagate through the caprock (Tong et al., 2023; Wasantha et al., 2019; Thiercelin, 1989; van Eekelen, 1982). However, the depth of penetration of the fracture into the bounding formation depends on the state of in-situ stress and should be assessed using numerical modelling approaches (Hu et al., 2022; Wang et al., 2015). Nevertheless, Zhang et al. (2018) argued that the minimum horizontal stress of the shale layer boundary is generally higher than the minimum horizontal stress measured in the reservoir sandstone and that the shale bounding layers or caprock could act as a stress barrier for the hydraulic fracture propagation (Zhang and Zhang, 2017; Adachi et al., 2010). However, the upper value of the minimum horizontal stress of the bounding shale layer could not be estimated in this study. According to Wileveau et al. (2007) and Zhang and Zhang (2017), the upper limit of the minimum horizontal stress should be calibrated with data from a leak-off test (LOT) or an extended leak-off test (XLOT). LOT and XLOT data at the depth of the shale caprock were not available. Therefore, a direct measurement of the minimum horizontal with a minifrac test at a depth of boundary shale layer is recommended to fully evaluate the fracture containment potential of the F–O tight gas.

Three types of natural fractures (NFs) were observed, with partial fractures appearing to be the predominant type of fracture in the reservoir. As shown in Fig. 10, all fracture types are stable under the current stress. However, when the differential horizontal stress exceeds 10 MPa hydraulic fractures intersecting NFs at angles between 60° and 90° can either cross the pre-existing NFs or induce dilatation, as highlighted by Zhou et al. (2015). Nevertheless, it should be noted that partial fractures are more likely to undergo dilatation compared to resistive fractures (Fu et al., 2015). In contrast, at low-stress differences, hydraulic fractures cause the NFs to slip and reactivate (Zhu et al., 2018).

6. Conclusions

In this study, a methodology was proposed to investigate the hydraulic fracturing potential of tight gas reservoirs through a detailed petrographic, fine migration, rock mechanics, fracture and geomechanical analysis. The results obtained showed that.

- K-means clustering improves reservoir characterisation by revealing heterogeneity and consequently facilitating petrographic and geomechanical analysis.
- At the critical velocity of 0.155 ml/min and below, the hydraulic fracturing fluid does not cause formation damage in the reservoir.
- The stress regime in the Bredasdorp Basin changes from normal faulting to a normal/strike-slip regime near the Agulhas fracture zone.
- The elastic properties obtained from the geomechanical tests revealed that the F–O gas field has a high degree of brittleness, which makes it a promising candidate for hydraulic fracturing. However, the contrast in fracture toughness between the pay zone and the bounding (caprock) formations indicates that the fracture may propagate through the caprock. However, the minimal horizontal of the shale bounding layer could arrest the propagation.
- Partial fractures appear to be the predominant fractures that will tend to propagate under the high differential stress in the reservoir.

Although this study sheds light on the potential application of hydraulic fracturing in the F–O gas field, there are certain questions that must be addressed. For example, the retention potential in the F–O reservoir is still uncertain and needs to be further investigated. Another critical task is to determine the optimal angle of approach for the intersection of HFs with NFs to formulate an efficient hydraulic fracturing design. Nevertheless, it seems that the F–O gas field is a promising candidate for hydraulic fracturing and could serve as a possible alternative energy solution amidst the ongoing debates on using hydraulic fracturing in South Africa.

CRediT authorship contribution statement

Sithembele Zangqa: Writing – review & editing, Writing – original draft, Methodology, Investigation, Formal analysis, Data curation, Conceptualization. **Eric Saffou:** Writing – review & editing, Supervision, Investigation, Conceptualization. **Raoof Gholami:** Writing – review & editing. **Udo Zimmermann:** Writing – review & editing. **Arshad Raza:** Writing – review & editing. **Musa S.D. Manzi:** Writing – review & editing, Supervision. **Ray Durrheim:** Writing – review & editing.

Data availability

The data that has been used is confidential.

Acknowledgments

The work presented was supported by NRF. We thank PetroSA for providing data for this project. The support of the DSI-NRF Centre of Excellence (CoE) for Integrated Mineral and Energy Resource Analysis (DSI-NRF CIMERA) towards this research is hereby acknowledged. Opinions expressed and conclusions arrived at are those of the author(s) and are not necessarily to be attributed to the CoE.

References

Abou-Sayed, A.S., 1978. No title. VDI-Ber. 313, 819–824.
Adachi, J.I., Detournay, E., Peirce, A.P., 2010. Analysis of the classical pseudo-3D model for hydraulic fracture with equilibrium height growth across stress barriers. Int. J. Rock Mech. Min. Sci. 47 (4), 625–639. https://doi.org/10.1016/j.ijrmms.2010.03.008.
Baniak, G.M., Gingras, M.K., Burns, B.A., Pemberton, S.G., 2015. Petrophysical characterisation of bioturbated sandstone reservoir facies in the upper jurassic ula formation, Norwegian north sea, europe. J. Sediment. Res. 85 (1), 62–81. https://doi.org/10.2110/jsr.2015.05.
Bate, K.J., Malan, J.A., De Wit, M.J., Ransome, I.G.D., 1992. Tectonostratigraphic evolution of the algoa, gamtoos and pletmos basins, offshore South Africa. Inversion Tectonics of the Cape Fold Belt, Karoo and Cretaceous Basins of Southern Africa, pp. 61–73.
Booth, P. W. K., & Shone, R. W. (n.d.). A review of thrust faulting in the Eastern Cape Fold Belt, South Africa, and the implications for current lithostratigraphic interpretation of the Cape Supergroup. www.elsevier.com/locate/jafrearsci.
Ben-Avraham, Z., Hartnady, C.J.H., Malan, J.A., 1993. Early tectonic extension between the Agulhas Bank and the Falkland Plateau due to the rotation of the Lafonia microplate. Earth and Planetary Science Letters 117 (1–2), 43–58.
Bill Grieser, & Jun Bray, H., 2007. Grieser2007. *Spe 106623*, *SPE 106623*, 1–6. Scrutton, R.A. and Dingle, R.V., 1976. Observations on the processes of sedimentary basin formation at the margins of southern Africa. In *Developments in Geotectonics* (Vol. 12, pp. 143-156). Elsevier.
Brown, R., Summerfield, M., Gleadow, A., Gallagher, K., Carter, A., Beucher, R., Wildman, M., 2014. Intracontinental deformation in southern Africa during the late cretaceous. J. Afr. Earth Sci. 100, 20–41. https://doi.org/10.1016/j.jafrearsci.2014.05.014.
Byrne, M., Rojas, E., Kandasamy, R., Gibb, A., 2014. Fines migration in oil and gas reservoirs: quantification and qualification through detailed study. SPE - European Formation Damage Conference, Proceedings, EFDC 1, 390–395. https://doi.org/10.2118/168150-ms.
Chen, Z., Yang, Z., Wang, M., 2018. Hydro-mechanical coupled mechanisms of hydraulic fracture propagation in rocks with cemented natural fractures. J. Petrol. Sci. Eng. 163 (January), 421–434. https://doi.org/10.1016/j.petrol.2017.12.092.
Chima, P., Baiyegunhi, C., Liu, K., Gwavava, O., 2018a. Diagenesis and rock properties of sandstones from the stormberg Group, Karoo Supergroup in the eastern cape province of South Africa. Open Geosci. 10 (1), 740–771. https://doi.org/10.1515/geo-2018-0059.
Chima, P., Baiyegunhi, C., Liu, K., Gwavava, O., 2018b. Petrography, modal composition and tectonic provenance of some selected sandstones from the molteno, elliot and clarens formations, Karoo Supergroup, in the eastern cape province, South Africa. Open Geosci. 10 (1), 821–833. https://doi.org/10.1515/geo-2018-0064.
Chisebe, K.B., 2017. *Exploring Potential Impacts of Hydraulic Fracturing (Fracking) on Groundwater Contamination in the Karoo: Perspectives on Institutional Capabilities in Water Management in South Africa* (Doctoral dissertation. University of the Witwatersrand, Faculty of Science, School of Geography, Archaeology & Environmental Studies.
Davies, N., 1997. Hydrocarbon Evolution of the Bredasdorp Basin, Offshore south africa: from Source to Reservoir.
De Wit, M.J., Ransome, I.G.D., 1992. Inversion tectonics of the Cape Fold Belt, Karoo and cretaceous basins of southern Africa. Proceedings of the Conference on Inversion Tectonics of the Cape Fold Belt, Cape Town, South Africa, 2-6 December 1991. Taylor & Francis.
Dou, Y., Hu, P., Zhu, R., 2021. Optimization of fracturing parameters for tight sandstone gas reservoirs. In: IOP Conference Series: Earth and Environmental Science, vol. 859. IOP Publishing, 012022, 1.
Duncan, R.A., Hooper, P.R., Rehacek, J., Marsh, J. and Duncan, A.R., 1997. The timing and duration of the Karoo igneous event, southern Gondwana. *Journal of Geophysical Research: Solid Earth*, *102*(B8), pp.18127-18138.
Duncan, R.A., 1981. Hotspots in the Southern Oceans - an absolute frame of reference for motion of the Gondwana continents. Tectonophysics 74 (1–2), 29–42. https://doi.org/10.1016/0040-1951(81)90126-8.
Folk, R.L., 1980. Petrology of Sedimentary Rocks. Hemphill publishing company.
Fu, P., Cruz, L., Moos, D., Settgast, R.R., Ryerson, F.J., 2015. Numerical investigation of a hydraulic fracture bypassing a natural fracture in 3D. In: *49th U.S. Rock Mechanics/Geomechanics Symposium* (P. ARMA-2015-671).
Godongwana, V., Groenewald, A., Poquioma, F., 2009. In: *Unconfined, Triaxial, and Hydrostatic Compression Testing, Indirect Tensile Strength Testing, and Petrologic and Petrophysical Analyses of Selected Core*Material.
Grieser, Bill, Jun Bray, H., 2007. Grieser2007. *Spe 106623, SPE 106623*, pp. 1–6.
Guo, T., Zhang, S., Zou, Y., Xiao, B., 2015. Numerical simulation of hydraulic fracture propagation in shale gas reservoir. J. Nat. Gas Sci. Eng. 26, 847–856. https://doi.org/10.1016/j.jngse.2015.07.024.
Haughton, S.H., Rossouw, P.J., Blignaut, J.J.G., 1953. *Results of an investigation into the possible presence of oil in Karroo rocks in parts of the Union of South Africa*. Mem. Geol. Surv. S. Afr. 45, 122.
Hibbeler, J., Garcia, T., Chavez, N., 2003. An integrated long-term solution for migratory fines damage. In: Proceedings of the SPE Latin American and Caribbean Petroleum Engineering Conference, pp. 152–162. https://doi.org/10.2118/81017-ms.
Hirsch, K.K., Bauer, K., Scheck-Wenderoth, M., 2009. Deep structure of the western South African passive margin - results of a combined approach of seismic, gravity and isostatic investigations. Tectonophysics 470 (1–2), 57–70. https://doi.org/10.1016/j.tecto.2008.04.028.
Hou, B., Chen, M., Jin, Y., Lin, B., Diao, C., Zhang, X., 2015. Optimum condition of hydraulic fracture-natural fracture interaction in shale block experiments. In: *49th U.S. Rock Mechanics/Geomechanics Symposium* (P. ARMA-2015-089).
Hu, Y., Gan, Q., Hurst, A., Elsworth, D., 2022. Hydraulic fracture propagation and interaction with natural fractures by coupled hydro-mechanical modeling. Geomechanics and Geophysics for Geo-Energy and Geo-Resources 8 (1). https://doi.org/10.1007/s40948-021-00307-9.
Hudson, P., Matson, R., 2012. Hydraulic Fracturing in Horizontal Wells. SPE. https://doi.org/10.15593/2224-9923/2013.6.11.
ISRM, 1983. Suggested methods for determining the strength of rock materials in triaxial compression: revised version. Int. J. Rock Mech. Min. Sci. Geomech. Abstr. 20 (6).
Joel, B.-A., Eswaran, P., 2015. Effect of bioturbation on reservoir rock quality of sandstones: a case from the Baram Delta, offshore Sarawak, Malaysia, 42 (Issue 2).
Johnston, S.T., 2000. The Cape Fold Belt and Syntaxis and the rotated Falkland Islands: dextral transpressional tectonics along the southwest margin of Gondwana. S J. Afr., Can Earth Soences 31 (Issue 1).
Jokat, W., Hagen, C., 2017. Tectonophysics crustal structure of the Agulhas ridge (south atlantic ocean): formation above a hotspot. Tectonophysics 716, 21–32. https://doi.org/10.1016/j.tecto.2016.08.011.
Kanin, E.A., Dontsov, E.V., Garagash, D.I., Osiptsov, A.A., 2021. A radial hydraulic fracture driven by a Herschel–Bulkley fluid. J. Non-Newtonian Fluid Mech. 295 (May), 104620 https://doi.org/10.1016/j.jnnfm.2021.104620.
Kathleen, M., Turner Jim, R., Florangel, E. and Roger, H., 2009. F-O Gas Field, Offshore South Africa-From Integrated Approach to Field Development. *Mode of access*.
Khan, I., Ismail, A., Ali, I., 2018. Identification of brittle and ductile zones in sandstone reservoir using well log analysis; A case study, Southern Indus Basin, Pakistan. IOP Conf. Ser. Mater. Sci. Eng. 414 (1) https://doi.org/10.1088/1757-899X/414/1/012021.
King, M., Member, H., David, A., Willis, G., Member, J., Shell, A., Houston, D.C., 1957. Mechanic of hydraulic fracture. Transac. AIME 210 (1), 153–168.
Kissinger, A., Helmig, R., Ebigbo, A., Class, H., Lange, T., Sauter, M., Heitfeld, M., Klünker, J., Jahnke, W., 2013. Hydraulic fracturing in unconventional gas reservoirs: Risks in the geological system, part 2: Modelling the transport of fracturing fluids, brine and methane. Environmental earth sciences 70, 3855–3873.
Kuhlmann, G., Adams, S., Campher, C., van der Spuy, D., di Primio, R., Horsfield, B., 2010. Passive margin evolution and its controls on natural gas leakage in the southern Orange Basin, blocks 3/4, offshore South Africa. Mar. Petrol. Geol. 27 (4), 973–992. https://doi.org/10.1016/j.marpetgeo.2010.01.010.
Kumar, R.R., Molenaar, M.M., Subbiah, S.K., 2022. Constraining tectonic components during a geomechanics-aided successful hydrofracturing campaign of tight gas exploration field. J. Pet. Explor. Prod. Technol. 12 (4), 1121–1128. https://doi.org/10.1007/s13202-021-01374-0.
Liu, P., Wang, Z., Lu, K., Zhang, Z., 2022. Effect of sandstone and mudstone thickness on artificial fracturing for hydrocarbon extraction from low-permeability reservoirs. Nat. Gas. Ind. B 9 (4), 411–425.
McKenzie, D., Jackson, J., 1983. The relationship between strain rates, crustal thickening, palaeomagnetism, finite strain and fault movements within a deforming zone. Earth and Planetary Science Letters 65 (1), 182–202.
McMillan, I.K., 2003. Foraminiferally defined biostratigraphic episodes and sedimentation pattern of the Cretaceous drift succession (Early Barremian to Late Maastrichtian) in seven basins on the South African and southern Namibian continental margin. South Afr. J. Sci. 99 (11–12), 537–576.
Mcmillan, I. K., Brink, G. J., Broad, D. S., & Maier, J. J. 1997. Late Mesozoic Sedimentary Basins off the South Coast of South Africa.

Muir, R.A., Bordy, E.M., Mundil, R., Frei, D., 2020. Recalibrating the break-up history of SW Gondwana: U–Pb radioisotopic age constraints from the southern Cape of South Africa. Gondwana Res. 84, 177–193. https://doi.org/10.1016/j.gr.2020.02.011.

Paton, D.A., 2006. Influence of crustal heterogeneity on normal fault dimensions and evolution: southern South Africa extensional system. J. Struct. Geol. 28 (5), 868–886. https://doi.org/10.1016/j.jsg.2006.01.006.

Pietersen, K., Chevallier, L., Levine, A., Maceba, T., Gaffoor, Z., Kanyerere, T., 2021. Prospective policy safeguards to mitigate hydrogeological risk pathways in advance of shale gas development in the Karoo basin, South Africa. Groundwater for sustainable development 12, 100499.

Rahman, M.M., Mteiri, S. Al, Suboyin, A., Haroun, M., 2021. Hydraulic fracture propagation and analysis in heterogeneous middle Eastern tight gas reservoirs: influence of natural fractures and well placement. ACS Omega 6 (1), 799–815. https://doi.org/10.1021/acsomega.0c05380.

Rathnaweera, T.D., Wu, W., Ji, Y., Gamage, R.P., 2020. Understanding injection-induced seismicity in enhanced geothermal systems: from the coupled thermo-hydro-mechanical-chemical process to anthropogenic earthquake prediction. Earth Sci. Rev. 205 (May 2019), 103182 https://doi.org/10.1016/j.earscirev.2020.103182.

Reeves, C., De Wit, M., 2000. Making ends meet in Gondwana: retracing the transforms of the Indian Ocean and reconnecting continental shear zones. Terra. Nova 12 (6), 272–280.

Saffou, E., Raza, A., Gholami, R., Croukamp, L., Elingou, W.R., van Bever Donker, J., Opuwari, M., Manzi, M.S.D., Durrheim, R.J., 2020. Geomechanical scharacterisation of CO2 storage sites: a case study from a nearly depleted gas field in the Bredasdorp Basin, South Africa. J. Nat. Gas Sci. Eng. 81 https://doi.org/10.1016/j.jngse.2020.103446.

Saffou, E., Raza, A., Gholami, R., Aci, C., Donker, J. van B., Salem, S., Zimmermann, U., Opuwari, M., Croukamp, L., Elingou, W.R., Chatterjee, T., Manzi, M.S.D., 2022. Full-scale simulation of a nearly depleted gas field in South Africa for carbon utilisation and storage. Greenhouse Gases: Sci. Technol. 22 (2022), 1–22. https://doi.org/10.1002/ghg.2160.

Rowsell, DM, de Swardt, A.M.J., 1976. Diagenesis in Cape and Karroo sediments, South Africa, and its bearing on their hydrocarbon potential. South African Journal of Geology 79 (1), 81–145.

Saffou, E., Gholami, R., Raza, A., Mahmoud, M., Manzi, M.S.D., Durrheim, R., 2023. A one-way coupled geomechanical model for CO 2 storage in faulted depleted gas reservoirs. Gas Sci. Eng. 120 (October), 205143 https://doi.org/10.1016/j.jgsce.2023.205143.

Salimzadeh, S., Zimmerman, R.W., Khalili, N., 2020. Gravity hydraulic fracturing: a method to create self-driven fractures. Geophys. Res. Lett. 47 (20), 1–10. https://doi.org/10.1029/2020GL087563.

Shone, R.W., Nolte, C.C., Booth, P.W.K., 1990. Pre-Cape rocks of the Gamtoos area-a complex tectonostratigraphic package preserved as a horst block. S. Afr. J. Geol. 93 (4), 616–621.

Simonis, H., & Sontundu, S., 2010. *Geological Well Completion Report.*Higgs, R., 2009. *Cretaceous 'USM'Reservoir, FO Gas Field, Offshore South Africa: Sedimentological Factors Affecting Economic*Viability.

Simonson, E.R., Abou-Sayed, A.S., Clifton, R.J., 1978. Containment of massive hydraulic fractures. Soc. Pet. Eng. AIME J. 18 (1), 27–32. https://doi.org/10.2118/6089-pa.

Stankiewicz, J., Parsiegla, N., Ryberg, T., Gohl, K., Weckmann, U., Trumbull, R. and Weber, M., 2008. Crustal structure of the southern margin of the African continent: Results from geophysical experiments. *Journal of Geophysical Research: Solid Earth*, *113*(B10).

Sun, G., Wang, Y., Jiang, Y., Pan, S., Zhang, S., Zhang, M., 2020. Provenance and tectonic setting of Paleogene sandstone in the center of the northern Qaidam Basin, China. J. Nat. Gas Geosci. 5 (5), 273–284. https://doi.org/10.1016/j.jnggs.2020.09.002.

Tang, H., Tang, H., He, J., Zhao, F., Zhang, L., Liao, J., Wang, Q., Yuan, X., 2021. Damage mechanism of water-based fracturing fluid to tight sandstone gas reservoirs: improvement of the Evaluation Measurement for Properties of Water-based Fracturing Fluid: SY/t 5107-2016. Nat. Gas. Ind. B 8 (2), 163–172. https://doi.org/10.1016/j.ngib.2020.09.016.

Tankard, A., Welsink, H., Aukes, P., Newton, R., Stettler, E., 2009. Tectonic evolution of the cape and Karoo basins of South Africa. Mar. Petrol. Geol. 26 (8), 1379–1412. https://doi.org/10.1016/j.marpetgeo.2009.01.022.

Thiercelin, M., 1989. Fracture toughness and hydraulic fracturing. Int. J. Rock Mech. Min. Sci. 26 (3–4), 177–183. https://doi.org/10.1016/0148-9062(89)91967-0.

Thomas, W.A., 1993. Low-angle detachment geometry of the late Precambrian-Cambrian Appalachian-Ouachita rifted margin of southeastern North America. Geology 21 (10), 921–924.

Tinker, J., de Wit, M., Brown, R., 2008. Mesozoic exhumation of the southern Cape, South Africa, quantified using apatite fission track thermochronology. Tectonophysics 455 (1–4), 77–93. https://doi.org/10.1016/j.tecto.2007.10.009.

Tong, Z., Ding, W., Wang, C., Li, C.F., 2023. Analogue modelling of subduction initiation: a review and perspectives. International Geology Review 1–43.

van Eekelen, H.A.M., 1982. Hydraulic fracture geometry: fracture containment in layered formations. Soc. Petrol. Eng. J. 22 (3), 341–349. https://doi.org/10.2118/9261-PA.

Wang, H.Y., 2019. Hydraulic fracture propagation in naturally fractured reservoirs: complex fracture or fracture networks. J. Nat. Gas Sci. Eng. 68 (June), 102911 https://doi.org/10.1016/j.jngse.2019.102911.

Wang, H., Liu, H., Wu, H.A., Wang, X.X., 2015. A 3D numerical model for studying the effect of interface shear failure on hydraulic fracture height containment. J. Petrol. Sci. Eng. 133, 280–284. https://doi.org/10.1016/j.petrol.2015.06.016.

Wang, W., Olson, J.E., Prodanović, M., Schultz, R.A., 2018. Interaction between cemented natural fractures and hydraulic fractures assessed by experiments and numerical simulations. J. Petrol. Sci. Eng. 167 (November 2017), 506–516. https://doi.org/10.1016/j.petrol.2018.03.095.

Wasantha, P.L.P., Konietzky, H., Xu, C., 2019. Effect of in-situ stress contrast on fracture containment during single- and multi-stage hydraulic fracturing. Eng. Fract. Mech. 205 (November 2018), 175–189. https://doi.org/10.1016/j.engfracmech.2018.11.016.

Wildman, M., Brown, R., Watkins, R., Carter, A., Gleadow, A., Summerfield, M., 2015. Post break-up tectonic inversion across the southwestern cape of South Africa: new insights from apatite and zircon fission track thermochronometry. Tectonophysics 654, 30–55. https://doi.org/10.1016/j.tecto.2015.04.012.

Wileveau, Y., Cornet, F.H., Desroches, J., Blumling, P., 2007. Complete in situ stress determination in an argillite sedimentary formation. Phys. Chem. Earth 32 (8–14), 866–878. https://doi.org/10.1016/j.pce.2006.03.018.

Will, T.M., Frimmel, H.E., 2018. Where does a continent prefer to break up? Some lessons from the South Atlantic margins. Gondwana Research 53, 9–19.

Winter, H.D.L.R., Venter, J.J. and Haughton, S.H., 1970. *Lithostratigraphic correlation of recent deep boreholes in the Karroo-Cape Sequence* (pp. 395-408). Soekor.

Xie, J., Huang, H., Ma, H., Zeng, B., Tang, J., Yu, W., Wu, K., 2018. Numerical investigation of effect of natural fractures on hydraulic-fracture propagation in unconventional reservoirs. J. Nat. Gas Sci. Eng. 54 (September 2017), 143–153. https://doi.org/10.1016/j.jngse.2018.04.006.

Xiong, D., Ma, X., 2022. Influence of natural fractures on hydraulic fracture propagation behaviour. Eng. Fract. Mech. 276 (PA), 108932 https://doi.org/10.1016/j.engfracmech.2022.108932.

Xu, W., Zhao, J., Rahman, S.S., Li, Y., Yuan, Y., 2019. A comprehensive model of a hydraulic fracture interacting with a natural fracture: analytical and numerical solution. Rock Mech. Rock Eng. 52 (4), 1095–1113. https://doi.org/10.1007/s00603-018-1608-9.

Yan, C., Chen, Y., Chen, T., Cheng, Y., Yan, X., 2022. Experimental study of hydraulic fracturing for unconsolidated reservoirs. Rock Mech. Rock Eng. 55 (6), 3399–3424.

Yang, K., Gao, D., 2022. Numerical simulation of hydraulic fracturing process with consideration of fluid–solid interaction in shale rock. J. Nat. Gas Sci. Eng. 102 (April), 104580 https://doi.org/10.1016/j.jngse.2022.104580.

Yang, Y., Siqueira, F.D., Vaz, A.S.L., You, Z., Bedrikovetsky, P., 2016. Slow migration of detached fine particles over rock surface in porous media. J. Nat. Gas Sci. Eng. 34, 1159–1173. https://doi.org/10.1016/j.jngse.2016.07.056.

Yaobin, S., Weiyong, L., Changchun, H., Erhu, B., 2020. Numerical simulation of the influence of natural fractures on hydraulic fracture propagation. Geofluids 2020. https://doi.org/10.1155/2020/8878548.

Zhang, Y., Zhang, J., 2017. Lithology-dependent minimum horizontal stress and in-situ stress estimate. Tectonophysics 703–704, 1–8. https://doi.org/10.1016/j.tecto.2017.03.002.

Zhang, S.C., Lei, X., Zhou, Y.S., Xu, G.Q., 2015. Numerical simulation of hydraulic fracture propagation in tight oil reservoirs by volumetric fracturing. Petrol. Sci. 12 (4), 674–682. https://doi.org/10.1007/s12182-015-0055-4.

Zhang, Y., Zhang, J., Yuan, B., Yin, S., 2018. In-situ stresses controlling hydraulic fracture propagation and fracture breakdown pressure. J. Petrol. Sci. Eng. 164 (January), 164–173. https://doi.org/10.1016/j.petrol.2018.01.050.

Zhang, J., Li, Y., Pan, Y., Wang, X., Yan, M., Shi, X., Zhou, X., Li, H., 2021. Experiments and analysis on the influence of multiple closed cemented natural fractures on hydraulic fracture propagation in a tight sandstone reservoir. Eng. Geol. 281 (October 2020), 105981 https://doi.org/10.1016/j.enggeo.2020.105981.

Zheng, H., Zhang, J., Qi, Y., 2020. Geology and geomechanics of hydraulic fracturing in the Marcellus shale gas play and their potential applications to the Fuling shale gas development. Energy Geosci. 1 (1–2), 36–46. https://doi.org/10.1016/j.engeos.2020.05.002.

Zhou, J., Huang, H., Deo, M. and Jiang, X., 2015. *A new physics-based modeling of multiple non-planar hydraulic fractures propagation. Unconventional Resources Technology Conference, San Antonio, Texas, 20-22 July*. URTEC-2170875-MS.

Zhu, G., Sousa, R., Abdulla, M.B., Abu Al-Rub, R., Sassi, M., 2018. Numerical investigation of the interaction between hydraulic fractures and nature fractures at reservoir scale. In: 2nd International Discrete Fracture Network Engineering Conference. D023S013R002.

Zoback, M.D., Barton, C.A., Brudy, M., Castillo, D.A., Finkbeiner, T., 2003. Determination of stress orientation and magnitude in deep wells. Int. J. Rock Mech. Min. Sci. 40, 1049–1076. https://doi.org/10.1016/j.ijrmms.2003.07.001.